Numerical Investigation of Vortex Onset in Supersonic Taylor–Couette Flow

Bénédicte Larignon[*]
University of Texas at Austin, Austin, Texas 78712
Stefan Wernz[†]
University of Arizona, Tucson, Arizona 85721
David B. Goldstein[‡]
University of Texas at Austin, Austin, Texas 78712
and
Hermann F. Fasel[§]
University of Arizona, Tucson, Arizona 85721

The compressible flow between concentric cylinders, in the case where the inner cylinder rotates and the outer one is at rest, has been computed using a pseudospectral/finite difference method. The onset of turbulence in rarefied supersonic gap flows for flywheel applications, and particularly the impact of surface roughness on the development of Taylor vortices, has been explored. An immersed boundary method using an external force field was employed to model the surface roughness. The Navier–Stokes code was validated against results from the literature for a supersonic wide-gap flow. To validate the immersed boundary method, the rotor wall was replaced by a smooth offset wall modeled with an external force field. Very good agreement with the analytical solution for steady Couette flow was achieved. The growth of Taylor vortices in a narrow gap with smooth walls was studied first. Then, the external force field was used to create a riblet on the rotor to investigate the influence of the roughness of the rotor on the flow and, more particularly, on the onset of the instability. The most interesting feature is the early appearance of vortices for Taylor numbers where the flow with smooth walls is in the subcritical regime.

Nomenclature

$c_{p,v}$	=	specific heat at constant pressure/volume
d	=	gap width
E	=	energy
Ec	=	Eckert number, $\equiv U_1^2/c_p T_2$
E_{IBM}	=	energy term used in immersed boundary method (IBM)
f	=	forcing term
J	=	number of points in radial direction
j	=	radial point number
K	=	highest azimuthal mode number
k	=	azimuthal mode number
M	=	Mach number, $\equiv U_1/\sqrt{(\gamma R T_2)}$
N	=	highest axial mode number
n	=	axial mode number
P	=	pressure
q_i	=	heat flux
Re	=	Reynolds number, $\equiv (\rho_2 U_1 R_1)/\mu_2$
$R_i^{n,k}$	=	coefficients $i = 1$–4 for Fourier mode n, k (density)
R_w	=	radius of virtual wall
$R_{1,2}$	=	radius of inner/outer cylinder
r	=	position in radial direction
T	=	temperature
Ta	=	Taylor number, $\equiv (\rho_2 U_1 d/\mu_2)\sqrt{(d/R_1)}$
$T_{1,2}$	=	temperature of inner/outer cylinder
t	=	time
U_1	=	tangential velocity of inner cylinder
u	=	axial velocity
V	=	velocity vector used in IBT method
v	=	radial velocity
w	=	azimuthal velocity
x_i	=	grid point
x_s	=	point of virtual surface
z	=	position in axial direction
α	=	negative constant in external force term
α_E	=	negative constant in source term for energy equation
β	=	negative constant in external force term
β_E	=	negative constant in source term for energy equation
γ	=	ratio of specific heats
δ_{ij}	=	Kronecker delta
θ	=	position in azimuthal direction
λ_z	=	axial wavelength
$\rho_{1,2}$	=	density of inner/outer cylinder
τ_{ij}	=	viscous stress
υ	=	kinematic viscosity
ω_i	=	linear growth rate of vortices

*Research Assistant, Department of Aerospace Engineering; larignonb@mail.utexas.edu. Student Member AIAA.

†Postdoctoral Researcher, Department of Aerospace and Mechanical Engineering; wernzs@email.arizona.edu.

‡Professor, Department of Aerospace and Engineering Mechanics; david@cfdlab.ae.utexas.edu. Member AIAA.

§Professor, Department of Aerospace and Mechanical Engineering; faselh@email.arizona.edu. Member AIAA.

I. Introduction

A FLYWHEEL system consisting of a spinning mass rotating around its axis is a compact, safe, low-maintenance, long-lasting energy storage device suitable for electric vehicles, or in mobile or stationary electric power supplies. Indeed, due to improved strength, stiffness, and thermal properties of composite materials, it is now possible to create flywheels that can sustain much higher rotation rates than previously attainable. Moreover, the new flywheels can use magnetic bearings to levitate the rotor, which, in turn, eliminate the frictional losses due to mechanical rollers. For many applications, a near vacuum can be sustained in the gap between the rotor and the stator, and, in these cases, the aerodynamic losses are

negligible. However, for some applications, this low pressure cannot be sustained, and the flywheel has to be run at higher pressures, perhaps all of the way into the continuum flow regime. The continuum flow induced by the rotation of the rotor is well known and referred to as a Taylor–Couette flow, which is an often-studied fluid dynamic problem prominent in the development of rotating machinery. Depending on the flow and geometric parameters, the fluid in the gap may be characterized by a variety of flow states ranging from free molecular to continuum, laminar to turbulent, and by the presence of steady or unsteady toroidal (Taylor) vortices. The various flow regimes influence the torque required to drive the rotor as well as the viscous heating of the surfaces. In the case of a flywheel, the appearance of vortices is detrimental to frictional energy loss and heating.

In incompressible flow, the development of the Taylor vortices can be predicted by means of the Taylor number, $Ta = Re(d/R_1)^{3/2}$, which is a nondimensional measure of the gap width d, compared to the rotor radius R_1, and is proportional to the Reynolds number, $Re \equiv U_1 R_1 / \nu_2$. In an incompressible flow, a surprisingly large variety of distinct Taylor vortex states can be identified.[1] As the Taylor number is increased, a simple laminar Couette flow may transition to one having either straight or sinuous Taylor vortices, unsteady vortices, or turbulent flow superimposed on Taylor-like vortices. In fact, the study of Taylor–Couette flows constitutes an important classic problem in fluid mechanics[2] with excellent analytical, experimental, and numerical work having been done on primary[3,4] and secondary instability growth,[5–7] on the transition process,[8] chaos,[9] etc. These flow-state changes correspond to torque changes and, if there are temperature differences, will directly translate into changes in heat transfer.

Fewer investigations have been published on the Taylor–Couette flow at supersonic speeds. Kao and Chow[10] studied the effect of Mach number, Reynolds number, and wall temperatures on the linear disturbance growth of the Taylor vortices for a wide gap. They found that for a rotating inner cylinder with the outer cylinder at rest, an increase in the temperature ratio between outer and inner cylinder wall stabilizes the flow, whereas an increase in Mach number destabilizes the flow. These findings were confirmed by Hatay et al.[11] who employed linear theory as well as direct numerical simulation (DNS) for computing both wide, R_1/R_2 small, and narrow, $R_1/R_2 \approx 1$, gap flows. They also determined that for a narrow-gap flow, an increase in Mach number has a stabilizing effect, contrary to the wide-gap flow. This stabilizing effect was attributed to the increased compressibility for higher Mach numbers, which also appears to be stabilizing for other supersonic shear flows such as boundary layers. For the wide gap, destabilizing centrifugal forces are more dominant and, thus, more than offset the dampening effect of compressibility.

Today, the effect of surface texturing on wall-bounded shear flows is still not fully understood, particularly for the case of supersonic (and turbulent) flow. The flywheel geometry with the ensuing transitional or turbulent gap flow may present an ideal setup for gaining insight into the relevant physical mechanisms for the shear flow over a ribbed surface. Furthermore, the presence of winding ridges on the composite rotor may be expected to cause heat flux concentrations on the stator at some fixed positions. Choi and Orchard[12] have carried out experiments and have found a 10% increase in the heat transfer coefficient to riblet surfaces compared with that of a smooth surface.

Textured surfaces such as riblets present a challenge for numerical simulations due to the complexity of the boundary geometry. In the present approach, the difficulty of body-fitted gridding for complex flow geometries is bypassed by employing the immersed boundary method (IBM). This method has been developed to simulate unsteady flows around complex boundaries by using an external force. The force field is only applied at points in the flow where the boundary is to be placed. The computational domain can then be simple, and a spectral, finite difference, or finite volume method can be used to resolve the flow. The method was initially developed by Peskin[13] to study the incompressible blood flow around a heart valve. Peskin noticed that if the locations of the boundary points are specified, the problem is simpler because the force at each point may be cal-

culated independently. Goldstein et al.[14] used a similar force field approach for modeling a no-slip flow boundary. Goldstein et al.[15] showed that a virtual solid surface approach allowed the study of fully turbulent incompressible flows in complex geometries, such as over riblets, using a spectral method and showed that the external force field required only a small computational overhead.

The numerical study of the continuum flow between the rotor and the stator, Knudsen number $Kn < 0.01$, is presented in this paper for the case of a small ratio of the gap width to the radius of the rotor (a narrow gap). The flow between the rotor and the stator is simulated using a compressible, temporal DNS code (or CTDNS code) developed at the University of Arizona.[16–18] One objective of our research was to compare the numerical results obtained with the CTDNS code with the experiments conducted by the Center for Electromechanics at the University of Texas at Austin (UT-CEM).[19] The simulation of the shear stress and heat flux at the walls was of particular interest because of their influence on the windage losses in the gap due to heating and friction. These results are presented in Ref. 20. The second and third objectives presented herein were to examine the onset of vortical flow and to implement an external force field in the code to simulate complex boundaries. The first step was a validation of the code and of the force field implemented in the code. The steady base flow profiles and the temporal growth rate of vortices in the DNS simulations were compared to the results from Hatay et al.[11] The results for an offset wall modeling the rotor boundary were first compared against the analytical solutions for an incompressible Couette flow and then against the numerical results obtained without the force field for the Taylor-vortex flow regime. The second step was to look at the growth of the Taylor vortices in a narrow gap. The last step was to implement a riblet on the rotor wall to observe its influence on the flow and on the onset of instability.

II. Computational Approach

A. Governing Equations

For computing the continuum flow inside the radial gap between the rotor and the stator of a high-speed flywheel, a highly accurate, compressible Navier–Stokes code is employed that has been developed at the University of Arizona. Details of the code can be found in Refs. 16–18. A brief overview will now be provided. For this code, the three-dimensional compressible Navier–Stokes equations are solved in conservative form, including the continuity equation, the momentum equations, and the energy equation formulated for total energy, $E = c_v T + \frac{1}{2} u_i u_i$,

$$\rho_{,t} + (\rho u_i)_{,j} = 0 \tag{1}$$

$$(\rho u_i)_{,t} + (\rho u_i u_j + p \delta_{ij} - \tau_{ij})_{,j} = f(x_i, t) \tag{2}$$

$$(\rho E)_{,t} + [\rho u_j (E + p/\rho) + q_i - \tau_{ij} u_i]_{,j} = f_E(x_i, t) \tag{3}$$

All flow variables are nondimensionalized by a reference velocity, length scale, density, and temperature. Additional constitutive relations are employed to close the governing equations, namely, the equation of state for ideal gas for computing the pressure p, the Newtonian fluid assumption for the viscous stress τ_{ij}, Fourier heat conduction for the heat flux q_j, and Sutherland's law for the dependence of viscosity and conductivity on the temperature. The forcing terms $f(x_i, t)$ and $f_E(x_i, t)$ added in Eqs. (2) and (3) will be discussed in Sec. II.B. The governing equations are solved in cylindrical coordinates inside the annular computational domain shown in Fig. 1 using a pseudospectral decomposition in the axial z and the azimuthal θ directions. In the simulations, flow variables are, thus, represented by a series of Fourier modes, for example, for the density,

$$\rho(r, z, \theta, t) = \sum_{n=0}^{N} \sum_{k=0}^{K} \left[R_1^{n,k}(r, t) \cos \frac{2\pi}{\lambda_z} nz \right.$$

$$+ R_2^{n,k}(r, t) \sin \frac{2\pi}{\lambda_z} nz \right] \cos k\theta + \left[R_3^{n,k}(r, t) \cos \frac{2\pi}{\lambda_z} nz \right.$$

$$\left. + R_4^{n,k}(r, t) \sin \frac{2\pi}{\lambda_z} nz \right] \sin k\theta \tag{4}$$

Although the CTDNS code is written for fully three-dimensional flow geometries, the flow is considered axisymmetric, $K = 0$, for all simulations presented in this paper. In radial direction r, sixth-order split compact differences are employed on a nonuniform grid with points clustered near the rotor and stator walls. An explicit, fourth-order Runge–Kutta scheme is used for time advancement. Whereas in the axial and azimuthal directions periodicity is assumed for all flow variables, in the radial direction, at the rotor/stator boundaries, no-slip conditions for the velocities and isothermal or adiabatic boundary conditions for the temperature can be imposed. The pressure at the boundaries is computed from the equation of state or from the radial momentum equation. Although the presently used compressible code is ideal for efficient and highly accurate computations of the transitional gap flow between concentric cylinders, different versions of the same code family are suited for computing various other aspects of the flywheel flow geometry. For example, the flow inside the end gaps can be computed using the spatial code version with high-order finite differencing in the axial direction.

The sixth-order split compact difference scheme allows the use of a variable radial grid. As the radial grid function, a stretching transformation from the book by Tannehill et al.[21] was chosen [Eq. (5.216), parameter $\beta = 1.03$]. A grid resolution study has been performed to determine the minimum number of points necessary to get an accurate solution (Fig. 2). A one-dimensional base flow with a Mach number of three has been chosen for the study. The final choice was a stretched grid with $J = 50$ mesh points, which is also employed for all other simulation cases presented in this paper (renormalized depending on the gap width d). Because the highest gradients are expected at the boundaries, the grid points are more closely spaced next to the walls than in the center of the gap (Fig. 2a).

B.   External Force for Modeling Immersed Wall Boundaries

A source term has been added to the Navier–Stokes equations (2) and (3) to allow for an external force and energy source field. The force has a magnitude and direction opposing the local flow at the surface such that the fluid is brought to rest on an element of the surface.[14] For an unsteady incompressible viscous flow, the calculation of these forcing terms is performed with a feedback scheme in which the velocity is used to iteratively determine the desired value. The force f at a point on the virtual surface x_s, a grid

point in our study, is given by Eq. (5) where $V = (u, v, w - U_1)$ is the velocity vector, t is the time, and α and β are negative constants,

$$f(x_s, t) = \alpha \int_0^t V(x_s, t') \, \mathrm{d}t' + \beta V(x_s, t) \tag{5}$$

The magnitude of the constants must be large enough so that the force field can track the changing flow, but small enough so that stability is ensured. The stability criterion depends partly on the method used to approximate the integral. In our simulations, the integral is calculated by using a Riemann sum. The time step used in the sum has been taken to be the time step used in the Runge–Kutta scheme, and α and β have the respective arbitrary values of -10 and -5, which drive the flow to steady state. The dimensions of α and β are $M/(L^3 T^2)$ and $M/(L^3 T)$, respectively. With these values, the code remained stable. The first term in Eq. (5) is sufficient to create a force field that will bring the flow to rest on the surface points, whereas the second, dissipative term represents the drag created by a small obstacle at x_s. In the present case, the force field is calculated at the points on the virtual wall and is smoothed over the points in the neighborhood of the virtual surface using a Gaussian distribution. As shown by Goldstein et al.,[14] the time integral and direct velocity feedback are adequate for solving the unsteady incompressible Navier–Stokes equations.

However, the compressible Navier–Stokes equations are considered here, and these equations must be solved simultaneously for the velocities, density, and energy. For that reason, in addition to the force field that is applied to the momentum equations, a heat source must also be applied to the energy equation. This source term brings the temperature at the immersed boundary to a predetermined value that can be that of the rotor or any other value. Both force field and heat sources adapt to the surrounding flow to bring the momentum and the temperature to the desired values at the virtual wall. The expression of the source term for the energy equation (3), is similar to the momentum force field,

$$f_E(x_s, t) = \alpha_E \int_0^t E_{\mathrm{IBM}}(x_s, t') \, \mathrm{d}t' + \beta_E E_{\mathrm{IBM}}(x_s, t) \tag{6}$$

where $E_{\mathrm{IBM}} = E - T_1(\gamma Ec)^{-1} - \frac{1}{2}U_1^2$. In the code, Eqs. (5) and (6) are treated in the exact same manner. This is to say that the coefficients α_E and β_E of Eq. (6) have the same magnitudes and dimensions as the ones in Eq. (5) and that the integral in Eq. (6) is also calculated using a Riemann sum with a time step taken to be equal to the time step used in the Runge–Kutta scheme.

C.   Code Validation

1.   Validation of Navier–Stokes Code for Supersonic Taylor–Couette Flow

The compressible Navier–Stokes code has been tested for numerous flow geometries,[16−18] including transitional and turbulent compressible boundary layers, and turbulent bluff-body wakes. As part of the present research, simulations of subsonic and supersonic Taylor–Couette flows inside wide and narrow gaps have been performed. For the compressible Taylor–Couette flow in a wide gap,
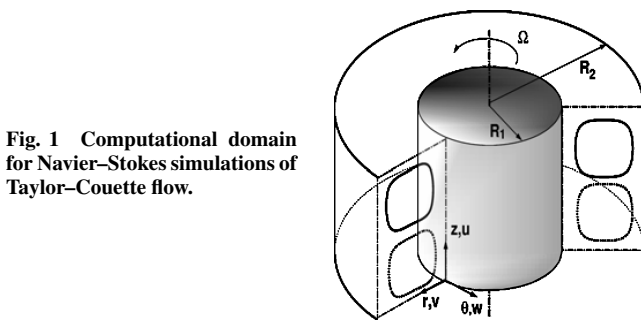

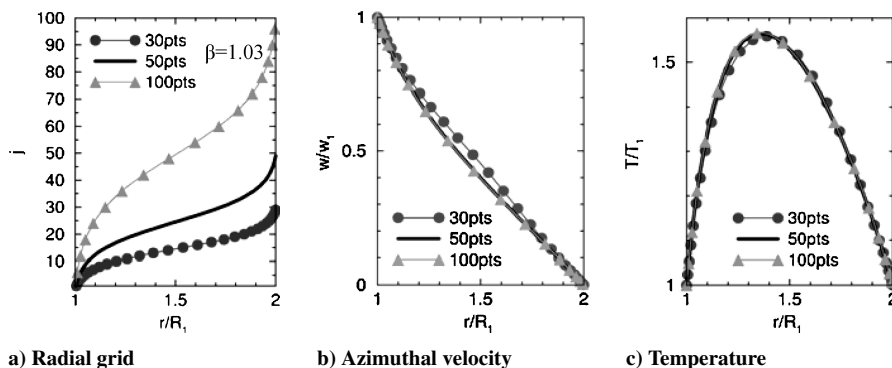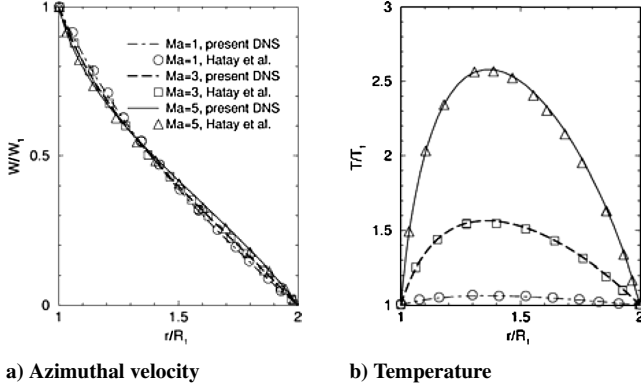Fig. 1   Computational domain for Navier–Stokes simulations of Taylor–Couette flow.
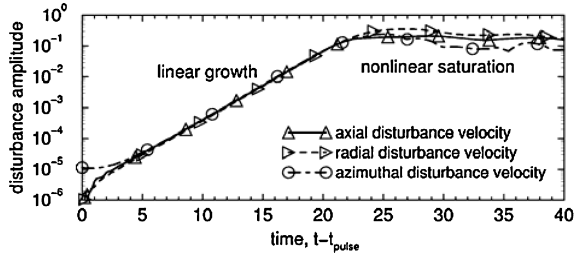

a) Radial grid   b) Azimuthal velocity   c) Temperature

Fig. 2   Compressible Couette flow between rotating inner cylinder and outer cylinder at rest with three different spatial resolution levels.

Table 1 Dimensional and nondimensional flow parameters

Case	Rotor temperature T_1, K	Stator temperature T_2, K	Stator pressure P_2, torr	Rotor radius R_1, m	Gap width, mm	Rotor tangential velocity U_1, m/s	Mach number M	Reynolds number Re	Taylor number Ta
1	380	400	10	0.2131	2.8	120	0.29	12980	19.5
2	380	400	10	0.21336	2.54	614	1.5	66500	100
3	380	400	5	0.2131	2.8	300	0.73	25300	38

a) Azimuthal velocity   b) Temperature

Fig. 3 Compressible Couette flow inside wide gap between rotating inner cylinder and outer cylinder at rest.

Fig. 4 Time development of Taylor vortex in response to small pulse disturbance at time $t = t_{\text{pulse}}$ for flow at $M = 1$ and $Ta = 800$.

results published in the literature are available for comparison and validation. One such benchmark case, with the inner cylinder rotating and the outer cylinder at rest, was computed by Kao and Chow[10] using linear theory and by Hatay et al.[11] using both linear theory and DNS.

For this case, the ratio of inner to outer cylinder radius is $R_1/R_2 = 0.5$, and no external force field is used. Rotor and stator are kept isothermally at temperature $T = 1$. The simulations are performed on a stretched radial grid using 50 points (Fig. 2a). In Fig. 3, the steady base flows computed with our code and from Hatay et al.[11] are compared for three different Mach numbers (rotor speeds). (For this validation case only, the nondimensional parameters M, Re, and Ta are defined using the velocity and the thermodynamic state quantities at the rotor wall.) With increased Mach number, the azimuthal velocity profile shown in Fig. 3a exhibits an increasingly pronounced S-shaped distortion due to compressibility effects enhanced by the action of the centrifugal force.[11] Also, due to internal friction heating inside the gap, the gap temperature increases dramatically for higher Mach numbers (Fig. 3b). For all three Mach numbers, our results are in excellent agreement with those by Hatay et al.[11] Although the steady base flow does not depend on the Reynolds number Re for Reynolds numbers above a certain threshold, the flow becomes unstable to centrifugal instabilities resulting in the development of axisymmetric counter-rotating vortices, so-called Taylor vortices. Shown in Fig. 4, for a case of $Ta = 800$ and $M = 1$, is the time development of a vortical disturbance in response to a small-amplitude perturbation in the density at time $t = t_{\text{pulse}}$. The axial wavelength of the disturbance is twice the gap width. Two higher axial Fourier modes, $N = 2$, are employed

for the simulation. After an initial adjustment, the vortical disturbance grows exponentially (linear growth) until $t - t_{\text{pulse}} \approx 22$ where nonlinear saturation sets in as the row of Taylor vortices becomes established. During the time period of linear growth, the temporal growth rate, $\omega_i = 0.52$, of the Taylor vortices perfectly matches the value published by Hatay et al.[11] (The temporal growth rate is defined as $\omega_i = 1/A(t) \cdot dA(t)/dt$, where $A(t)$ represents a measure of the vortex strength, for example, maximum disturbance velocity in the axial, radial, or azimuthal direction.)

2. Validation of IBM for Offset Wall

For validating the proper implementation of the IBM in the CTDNS code, a laminar Couette flow has been computed using the external force in the Navier–Stokes equations to simulate an offset virtual wall inside the computational domain. For the steady incompressible Couette flow between concentric cylinders, analytical solutions are readily available[22] for both the velocity,

$$w(r) = U_1 \frac{R_2/r - r/R_2}{R_2/R_w - R_w/R_2} \quad (7)$$

and the temperature,

$$T(r) = T_1 + \frac{\mu U_1^2}{\kappa} \frac{R_2^4}{R_2^4 - R_w^4} \left(1 - \frac{R_w^2}{r^2}\right) \left[1 - \frac{\ell_n(r/R_w)}{\ell_n(R_2/R_w)}\right]$$
$$+ (T_2 - T_1) \frac{\ell_n(r/R_w)}{\ell_n(R_2/R_w)} \quad (8)$$

The numerical results using the IBM have been compared to the analytical results for case 1 in Table 1. In Eqs. (7) and (8), the left boundary where $u = U_1$ and $T = T_1$ is at the location of the virtual wall, R_w. For that reason, the analysis should only look at the points between the offset wall and the stator. In the test case, the virtual wall is situated at the 16th grid point, which corresponds to a distance of $1.002R_1$, or 9% of the gap width, from the rotor. First, the azimuthal velocity and temperature profiles of the laminar Couette flow have been compared to the analytical results given by Eqs. (7) and (8). Because these two equations are valid for an incompressible flow, the parameters in the calculations have been chosen such that the Mach number is smaller than 0.3. Except for that constraint, the parameters of the flow have been selected to be within the range of the experimental cases run by UT-CEM (case 1 in Table 1). Finally, the properties of nitrogen have been chosen to model the gas inside the gap. The nondimensional parameters implemented in the code, the Mach number, the Reynolds number, as well as the Taylor number, are also presented in Table 1 (case 1).

As seen in Fig. 5, the numerical tangential velocity w is within 1% of the analytical solution, the largest deviation being at about $1.0025R_1$. The match is very good between the centerline and the stator, but closer to the virtual wall the numerical solution slightly deviates from the analytical solution, which is nearly linear (close up Fig. 5b). One of the reasons for this deviation, as von Terzi et al.[23] pointed out, may be that the addition of the immersed boundary method in the code can reduce the near-wall accuracy of the high-order scheme used in the radial direction. Moreover, the present technique, when computing a wall-normal gradient, uses points to the left of the virtual wall, which can also produce an incorrect value for the derivative. One can expect a better agreement between the numerical simulations and the analytical solutions if the condition
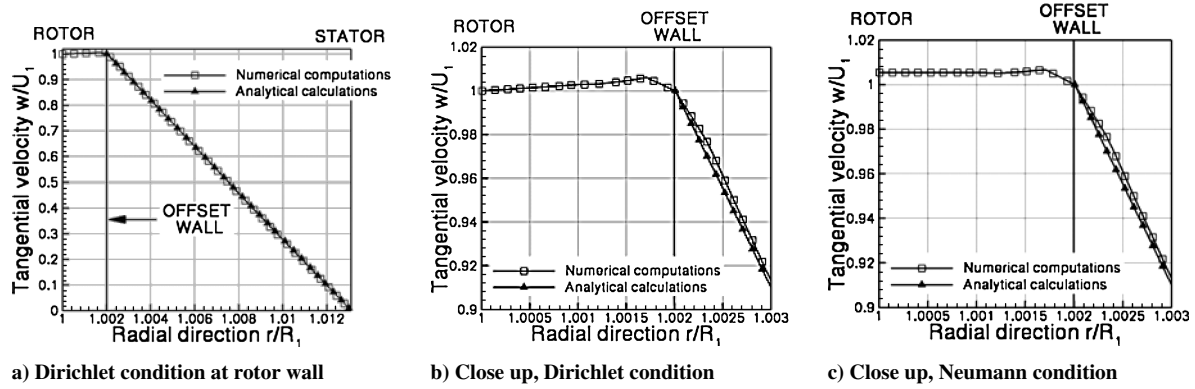
a) Dirichlet condition at rotor wall   b) Close up, Dirichlet condition   c) Close up, Neumann condition

Fig. 5   Laminar Couette flow: comparison of tangential velocity w from numerical solution and from analytical solution.
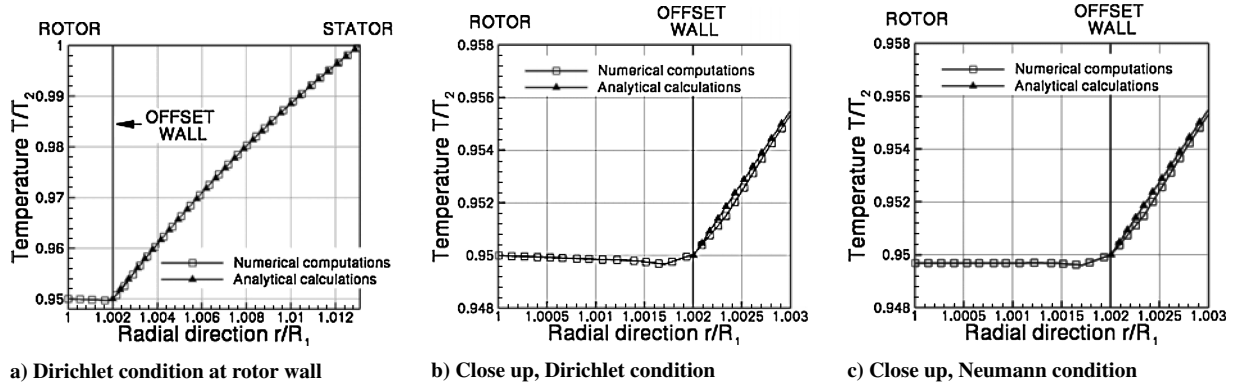

a) Dirichlet condition at rotor wall   b) Close up, Dirichlet condition   c) Close up, Neumann condition

Fig. 6   Laminar Couette flow: comparison of temperature T from numerical solution and from analytical solution.

applied at the rotor wall is less restrictive than a Dirichlet condition. For that reason, a different run has been made with a Neumann condition at the rotor wall (Fig. 5c). However, this different boundary condition at the rotor has a negligible influence on the values of the tangential velocity near the offset wall (cf. Figs. 5b and 5c). Fortunately, the accuracy near the virtual wall is not crucial in this study, and for the following runs the immersed boundary method with Dirichlet conditions is used as presented here.

A similar study has been made for the temperature. As seen in Fig. 6a, the numerical solution for the temperature agrees well with the analytical solution near the stator but diverges slightly from the analytical solution in the vicinity of the offset wall. When the cases where a Dirichlet condition and where a Neumann condition is applied at the rotor wall are compared (Figs. 6b and 6c), a similar behavior as for the tangential velocity (Figs. 5b and 5c) is observed. The flow inside the gap between the offset wall and the stator is hardly modified by the boundary condition at the rotor.

The numerical solution matches the analytical solution quite well in the case of an incompressible flow inside the gap, although some improvements could be made. One way of improving the numerical results would be to employ a force field throughout the region between the rotor and the offset wall to force a flow in the azimuthal direction.[15] In conjunction with a Neumann condition at the rotor, this small azimuthal flow would probably straighten the tangential velocity profile near the offset wall and, thus, provide a better agreement with the analytical solution. The same result may also be attained for the temperature by using a heat source/sink throughout the gap between the rotor and the offset wall. Some other solutions using correction methods for high-order immersed boundaries have been summarized and studied by von Terzi et al.[23] and by Linnick and Fasel.[24]

III.   Results

A.   Supersonic Taylor–Couette Flow in Narrow Gap Between Rotor and Stator of Flywheel

The growth of Taylor vortices was observed in direct numerical simulations of spin tests with the CEM flywheel system where the

Table 2   Parameters for DNS of Taylor–Couette flow at $M = 2$ inside radial gap[a] of CEM flywheel

Case	5 torr	10 torr	20 torr
Ta	45	92	255
M	1.94	1.81	2.01
T_1	306 K	321 K	Adiabatic
T_2	334 K	383 K	311 K

[a]Gap width $d = 0.1$ in. for all three cases.

gap between rotor and stator was narrow.[19] The rotor of the device had a radius of $R_1 = 21$ cm, the radial gap was on the order of $d = 2.5$ mm, depending on the rotor speed. Despite high rotor speeds of $M \approx 2$, the low pressure and narrow gap width resulted in very low Taylor numbers, and Taylor vortex flow was only expected for gap pressures on the order of 5 torr and above. Results from three simulations for gap pressures of 5, 10, and 20 torr, respectively, will now be presented. These simulations are axisymmetric, and no external force field is used. The flow parameters for the three cases are listed in Table 2.

For each case, the flow response to a small-amplitude disturbance was investigated with a parameter study for which the axial wavelength λ_z was varied. For the simulations in the parameter study, only two higher axial Fourier modes ($N = 2$) are computed. In radial direction, $J = 50$ mesh points are used. The result of this study is shown in Fig. 7 where the linear growth rate is plotted vs axial wavelength. For all three cases, the flow is unstable (growth rate $\omega_i > 0$) over a range of axial wavelengths. However, both the maximum growth rate and the range of wave numbers for which the flow is unstable increase with increased gap pressure. This is because an increase in gap pressure leads to an increase in density ρ; a decrease in kinematic viscosity ν; and, thus, an increase in Taylor number Ta. Consequently, the flow becomes more unstable for higher gap pressures. The maximum disturbance growth in all three cases was observed for an axial wavelength that is approximately 1.6 times the gap width d. For increased gap pressure, the disturbance not only exhibits a higher growth rate but also saturates at a

higher-amplitude level. This can be seen from simulations with a higher axial resolution, $N = 8$, for an axial domain width of $3.2d$ and for pressure levels of 5, 10, and 20 torr. Results are shown in Fig. 8 where the velocity field of the steady flow inside the gap at saturation level is plotted for the three cases. Whereas for low gap pressure (Fig. 8a) the resulting Taylor vortices are very weak, they significantly gain strength as the pressure is increased to 10 and 20 torr (Figs. 8b and 8c).

B. Comparison of DNS of Supersonic Taylor–Couette Flow With and Without Immersed Boundary Method

In this section, results from a DNS using an external force to model an offset rotor wall in the case of a supercritical, compressible flow are presented. For the simulation, the tangential velocity at the rotor $U_1 = 614$ m/s; the rotor radius $R_1 = 0.21336$ m; and the non-dimensional parameters are $M = 1.5$, $Re = 66,500$, and $Ta = 100$. All of the other parameters are presented in Table 1 under case 2. The temperature contours for case 2 with the offset wall are compared to the temperature contours obtained without the external force field in a smaller gap of the same width as the gap between the offset wall and the stator. As seen in Fig. 9, the line contours with and without the external force field agree well. This provides the confidence for employing the immersed boundary method to model riblets at the rotor wall.
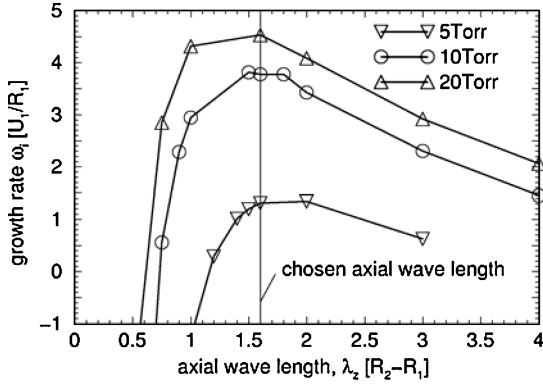
Fig. 7 Dependence of linear growth rate on axial wavelength and gap pressure.

C. DNS of Supersonic Flow Over Riblets at Rotor Wall

The interest in studying a riblet on the walls is twofold. First, the walls of the rotor and the stator are not completely smooth in practice. In fact, the fiber-wound rotor used in the experiments has azimuthal perturbations on the order of 0.5 mm. Given that the gap size is about 2.5 mm, the surface roughness at the rotor can extend up to 20% of the gap width. Such perturbations may present some bumps that can be large enough to influence the flow in the gap, given the small size of the gap in the first place. Moreover, the present code can be used to simulate three-dimensional flows, and
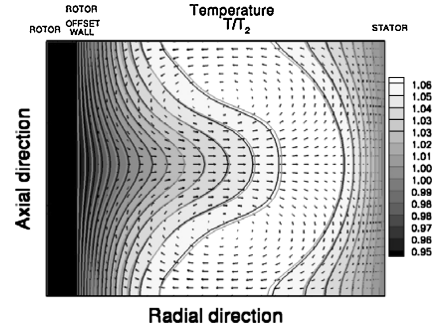
Fig. 9 Comparison of temperature fields from DNS with offset rotor wall (black contour lines and gray-scale contours) and DNS with Dirichlet boundary at same location (light gray contour lines), overlayed with v and w velocity vectors.
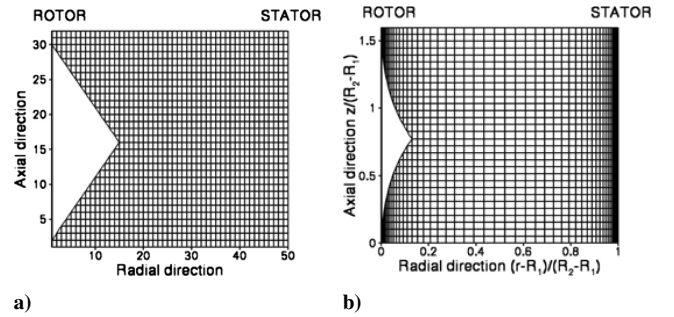
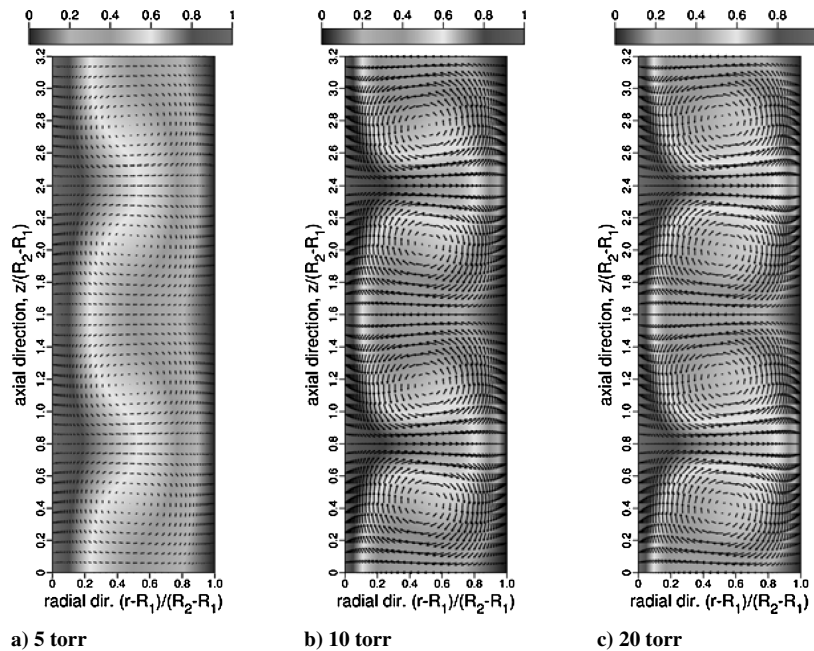**Fig. 10 Riblet geometry on a) unstretched and b) stretched grid.**

Fig. 8 Comparison of Taylor vortex flow at $M = 2$ for different pressure levels inside narrow radial gap of CEM flywheel. Shown are vector fields for radial/axial velocity components overlying gray-scale contours of azimuthal velocity.
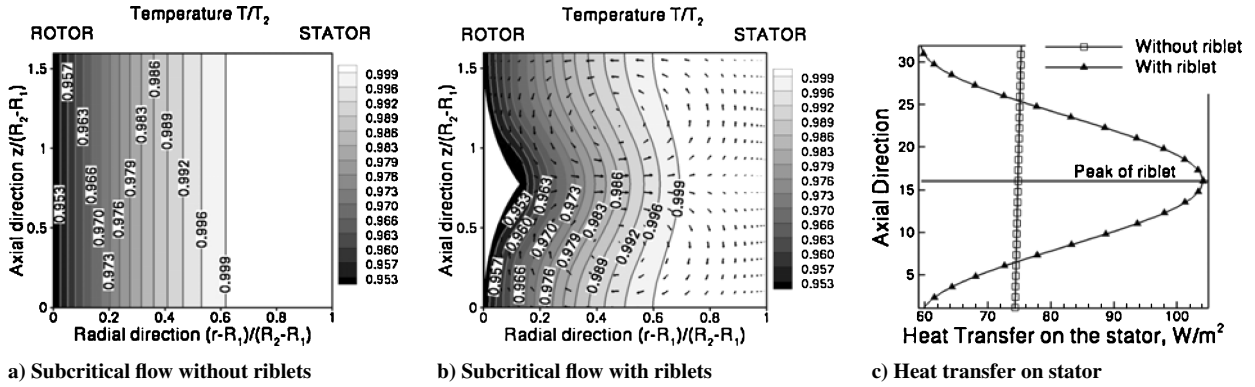
a) Subcritical flow without riblets   b) Subcritical flow with riblets   c) Heat transfer on stator

Fig. 11 Temperature contours for subcritical flow, $Ta = 38$, without and with riblet in the (r, z) plane and accompanying v and w velocity vectors; also shown is comparison of heat transfer on stator for both cases.
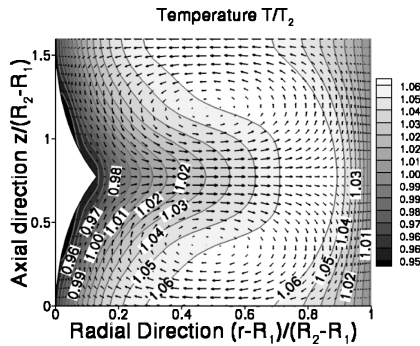

Fig. 12 Temperature contours for supercritical flow with riblet in (r, z) plane and accompanying v and w velocity vectors having length-to-magnitude ratio equal to one-third of value for vectors in subcritical simulation of Fig. 11.

the newly developed capability to model riblets will provide a tool to study the compressible turbulent flow over riblets. In this work, different runs have been made with a riblet on the rotor wall. The first set was run for a subcritical flow with a Taylor number of 38, whereas the second set was run for a supercritical flow. First, the geometry of the riblet is briefly discussed, and then the results for the subcritical and supercritical runs are presented.

1. Riblet Geometry

For implementation convenience, the surface of the riblet has been chosen to pass through grid points, even though the roughness at the wall can not be assumed to be a regular geometric shape. The basic shape has been chosen to be a triangle on a uniform grid, but, due to the stretching of the grid in the radial direction, the shape of the riblet is cusped. The riblet extends to the 15th grid point in the radial direction and from the 2nd to the 30th point in the axial direction, for a spectral space represented by 32 physical points. The riblet geometry on the unstretched and on the stretched grid is presented in Fig. 10 for one axial period. Note that, due to the assumed periodicity in axial direction, in fact, an infinite row of riblets is simulated.

2. Subcritical Flow Results

The aim for this simulation was to determine if the presence of riblets in a subcritical flow could induce transition from a Couette to a Taylor vortex flow. A subcritical flow with a $Ta = 38$ based on the gap between the rotor and the stator is considered. All of the parameters for this case are listed in Table 1 under case 3. Moreover, in the Sutherland equation for the viscosity, a modified reference dynamic viscosity of 1.066×10^{-5} N/m^2 was used instead of the customary reference value of 1.663×10^{-5} N/m^2 for nitrogen. This value was chosen so that the Taylor number is still barely subcritical. The remaining two nondimensional parameters are $M = 0.73$

and $Re = 25{,}300$. Temperature contours for the runs with and without riblets are shown in Figs. 11a and 11b, respectively. In the present case, riblets destabilize the flow, and Taylor vortices are observed in the gap. We note that in the case of an incompressible two-dimensional laminar channel flow,[25] no such vortices are observed in the presence of riblets.

A cold spot can be observed at the tip of the riblet shown in Fig. 11b, and, due to the presence of the vortices, the fluid gets colder in parts of the center region of the gap. This result demonstrates that riblets on the rotor wall can force the development of vortices in the otherwise subcritical flow. The heat flux at the stator wall for both runs, with and without riblets, is presented in Fig. 11c. In Fig. 11c, a clear increase in the heat flux can be seen at the axial position of the tip of the riblet.

3. Supercritical Flow Results

Finally, a supercritical run with riblets on the rotor wall has been made. For the simulation, the tangential velocity at the rotor is $U_1 = 614$ m/s; the rotor radius is $R_1 = 0.21336$ m; and the nondimensional parameters are $Ma = 1.5$, $Re = 66{,}500$, and $Ta = 100$. The temperature contours obtained in this case, however interesting, cannot be compared to any other data at present. In Fig. 12, the temperature contours are similar to the contours obtained in Fig. 9.

IV. Conclusions

In this paper, we have presented and validated a computational approach for investigating compressible Taylor–Couette flows at supersonic speeds. When an immersed boundary method is incorporated into the code that employs an external force field to impose no-slip and no-penetration conditions inside the computational domain, complex boundary geometries such as riblets can be modeled. The immersed boundary method was validated by comparing DNS results for an offset rotor wall inside the computational domain against DNS results with the rotor wall at the domain boundary. Aside from a slight discrepancy near the rotor wall, very good agreement was achieved between the two approaches. The implementation of riblets on the rotor wall was oriented toward future work that could be done with this code. For that reason, the work presented in this paper is only a first step, not a comprehensive study. However, some interesting trends can be observed from the few preliminary simulations with riblets. The most interesting feature is the early development of Taylor vortices in the subcritical flow regime. In the future, more detailed and systematic investigations of the effect of riblets on the Taylor–Couette flow will be conducted.

References

[1]Di Prima, R. C., and Swinney, H. L., "Instabilities and Transition in Flow Between Concentric Rotating Cylinders," *Hydrodynamic Instabilities and*

the Transition to Turbulence, edited by H. L. Swinney and J. P. Gollub, Topics in Applied Physics, Vol. 45, Springer-Verlag, New York, 1987, pp. 139–180.

[2]Schlichting, H., *Boundary Layer Theory*, 7th ed., translated by J. Kestin, McGraw–Hill, New York, 1979, Chap. 5.

[3]Taylor, G. I., "Stability of a Viscous Liquid Contained Between Two Rotating Cylinders," *Philosophical Transactions of the Royal Society of London, Series A: Mathematical and Physical Sciences*, Vol. 223, Feb. 1923, pp. 289–343.

[4]Davey, A., "The Growth of Taylor Vortices in Flow Between Rotating Cylinders," *Journal of Fluid Mechanics*, Vol. 14, 1962, pp. 336–368.

[5]Davey, A., Di Prima, R. C., and Stuart, J. T., "On the Instability of Taylor Vortices," *Journal of Fluid Mechanics*, Vol. 31, No. 1, 1968, pp. 17–52.

[6]Jones, C. A., "Nonlinear Taylor Vortices and Their Stability," *Journal of Fluid Mechanics*, Vol. 102, 1981, pp. 249–261.

[7]Jones, C. A., "The Transition to Wavy Taylor Vortices," *Journal of Fluid Mechanics*, Vol. 157, 1985, pp. 135–162.

[8]Coles, D., "Transition in Circular Couette Flow," *Journal of Fluid Mechanics*, Vol. 21, No. 3, 1965, pp. 385–425.

[9]Streett, C. L., and Hussaini, M. Y., "A Numerical Simulation of the Appearance of Chaos in Finite-Length Taylor–Couette Flow," *Applied Numerical Mathematics*, Vol. 7, No. 1, 1991, pp. 41–71.

[10]Kao, K.-H., and Chow, C.-Y., "Linear Stability of Compressible Taylor-Couette Flow," *Physics of Fluids A*, Vol. 4, No. 5, 1992, pp. 984–996.

[11]Hatay, F. F., Biringen, S., Erlebacher, G., and Zorumski, W. E., "Stability of High-Speed Compressible Rotating Couette Flow," *Physics of Fluids A*, Vol. 5, No. 2, 1993, pp. 393–404.

[12]Choi, K. S., and Orchard, D. M., "Turbulence Management Using Riblets for Heat and Momentum Transfer," *Experimental Thermal and Fluid Science*, Vol. 15, No. 2, 1997.

[13]Peskin, C. S., "Flow Patterns Around Heart Valves: A Digital Computer Method for Solving the Equations of Motion," Ph.D. Dissertation, Dept. of Physiology, Albert Einstein College of Medicine, Yeshiva Univ., July 1972.

[14]Goldstein, D. B., Handler, R., and Sirovich, L., "Modeling a No-Slip Flow Boundary with an External Force Field," *Journal of Computational Physics*, Vol. 105, No. 2, 1993, pp. 354–366.

[15]Goldstein, D. B., Handler, R., and Sirovich, L., "Direct Numerical Simulation of Turbulent Flow over a Modeled Riblet Covered Surface," *Journal of Fluid Mechanics*, Vol. 302, 1995, pp. 333–376.

[16]Balzer, W., "Investigation of Supersonic Wakes Using Temporal Direct Numerical Simulations," Ph.D. Dissertation, Inst. of Aerodynamics and Gas Dynamics, Univ. of Stuttgart, Stuttgart, Germany, 2003.

[17]Sandberg, R., "Numerical Investigation of Transitional and Turbulent Supersonic Axisymmetric Wakes," Ph.D. Dissertation, Dept. of Aerospace and Mechanical Engineering, Univ. of Arizona, Tucson, AZ, 2004.

[18]Sandberg, R., and Fasel, H., "Numerical Investigation of Transitional Supersonic Axisymmetric Wakes," *Journal of Fluid Mechanics* (submitted for publication).

[19]Hahne, J. J., Werst, M., Penney, C., Liu, H. P., O'Harden, J., and Bogard, D., "Measurement of Windage Losses and Temperature Distribution for a High Speed Composite Rotor in a Stator Assembly at Low Air Pressures," Paper 2003-47117, American Society of Mechanical Engineers, New York, July 2003.

[20]Larignon, B., Marr, K., and Goldstein, D., "Monte Carlo and Navier–Stokes Simulations of Compressible Taylor–Couette Flow," *Journal of Thermophysics and Heat Transfer*, Vol. 20, No. 3, 2006, pp. 544–551.

[21]Tannehill, J., Anderson, D., and Pletcher, R., *Computational Fluid Mechanics and Heat Transfer*, 2nd ed., Taylor and Francis, New York, 1997, p. 335.

[22]White, F. M., *Viscous Fluid Flow*, 2nd ed., McGraw–Hill, New York, 1991, pp. 110–112.

[23]von Terzi, D., Linnick, M., Seidel, J., and Fasel, H., "Immersed Boundary Techniques for High-Order Finite Difference Methods," AIAA Paper 01-2918, June 2001.

[24]Linnick, M., and Fasel, H., "A High-Order Immersed Boundary Method for Unsteady Incompressible Flow Calculations," AIAA Paper 2003-1124, Jan. 2003.

[25]Choi, H., Moin, P., and Kim, J., "On the Effect of Riblets in Fully Developed Laminar Channel Flows," *Physics of Fluids A*, Vol. 3, No. 8, 1991, pp. 1892–1896.